Transport in Porous Media (2021) 140:493–509
https://doi.org/10.1007/s11242-021-01690-3

Reducing User Bias in X-ray Computed Tomography-Derived Rock Parameters through Image Filtering

Ellen P. Thompson[1] · Kira Tomenchok[1] · Tyler Olson[1] · Brian R. Ellis[1]

Received: 30 April 2021 / Accepted: 17 September 2021 / Published online: 6 October 2021

Abstract

Accurate representation of pore space is essential for predicting fluid flow through subsurface porous media. Pore volume fraction, geometry, and topology determine transport characteristics at the pore scale and are used to make upscaled projections about reservoir behavior. X-ray computed tomography (XCT) allows for nondestructive 3D imaging of rock core samples and can therefore provide valuable information about the pore network in situ, but segmentation of XCT datasets into pore and mineral space is not trivial. In this study, three filters (contrast enhancement, noise reduction, and beam hardening correction) were applied to XCT datasets of rock core samples prior to training class definition for machine learning-based segmentation. Porosities derived from segmented datasets with and without filtering were compared and were validated with experimental values. XCT-derived porosity had reduced variance and was closer to experimental data when all three filters were applied. A case study of one rock core sample compared pore size distribution and simulated permeability to experimental data. Computational fluid dynamics simulations of flow through the pore network using OpenFOAM showed improved consistency in permeability values when all three filters had been applied. This suggests that the application of these filters prior to machine learning training class definition can improve the reproducibility of the segmentation results and reduce user bias, thereby increasing confidence in digitally derived rock parameters. Reliable initial porosity and permeability data are critical for improving fluid transport and fate projections in a broad range of subsurface systems.

Article Highlights .

- **Filtered datasets were less affected by user bias in definition of training classes**
- **Image filtering before segmentation improved consistency of simulated permeability**
- **Image filtering improved reproducibility of digitally derived rock parameters**

✉ Brian R. Ellis
brellis@umich.edu

[1] Department of Civil and Environmental Engineering, University of Michigan, 1351 Beal Ave, Ann Arbor, MI 48109, USA

Keywords X-ray computed tomography · Image filtering · Porous media characterization · Porosity · Permeability

1 Introduction

Reliable prediction of fluid flow through the subsurface is essential for numerous applications including subsurface energy technologies such as geothermal energy production, enhanced oil recovery, and geologic carbon sequestration. In systems where percolation through porous media dominates transport, core sample porosity is a primary characteristic that is used to predict upscaled reservoir parameters including permeability and flow dynamics and is a starting point for forecasting changes in formation behavior over time (Hommel et al. 2018; Ma 2015; Mostaghimi et al. 2013). Consistent, accurate determination of core porosity is therefore an imperative first step in modeling fluid transport in these systems.

X-ray computed tomography (XCT) allows nondestructive 3D imaging of rock material, making it an exceedingly useful tool for visualizing pore structures in situ. XCT imagery can provide geometric and topological information about the pore space that is crucial to predicting flow behavior in porous media, like pore throat size and pore connectivity (Bazaikin et al. 2017; Lindquist et al. 2000). The rise in availability of bench-scale XCT instruments has led to great advances in 3D characterization of geomaterials (Wildenschild and Sheppard 2013). Yet, reliable segmentation of XCT datasets into pore- and non-pore voxels, or individual mineral species, remains challenging. Traditional thresholding-based approaches to segmentation (e.g., global thresholding, watershed, and hysteresis) are sensitive to user bias (Iassonov et al. 2009). Ample research into the efficacy of various segmentation methods suggests that the optimal segmentation technique would minimize user supervision to reduce the influence of user subjectivity (Deng et al. 2016; Iassonov et al. 2009; Leu et al. 2014; Pini and Madonna 2016). Machine learning has therefore gained popularity as a method for XCT segmentation and analysis.

Trainable Weka Segmentation (TWS) is an open-source machine learning tool developed for Fiji (Schindelin et al. 2012) that leverages multiple image parameters to segment a dataset based on user-defined training classes (Arganda-Carreras et al. 2017). Originally developed for biological sciences research, TWS is also very useful in geoscience applications because it can segment large 3D datasets efficiently and with reduced user oversight. It has been used, for example, for classification of wetting phases in XCT scans of saturated reservoir rock (Alhammadi et al. 2018), as well as for in situ contact angle and fluid–fluid interfacial angle measurements (Garfi et al. 2020). Others have used TWS to determine crystal size distribution from scanning electron microscope (SEM) images of volcanic rock (Lormand et al. 2018).

Machine learning reduces subjectivity but does not completely eliminate user bias from the segmentation process; a classified dataset is only as good as its training data. Segmentation of the same core with different input training data can result in variable overall porosity estimates. Prior work suggests that other downstream parameters, including permeability, are even more sensitive than porosity to differences in the initial binary segmentation (Leu et al. 2014). It is therefore critical to improve the reproducibility of initial segmentation in order to make meaningful predictions of flow and transport through a rock system from XCT sample data.

Image filtering of XCT datasets can reduce the impact of scan artifacts on the segmentation process. Binary classification of the XCT dataset into pore space and non-pore space is complicated by the presence of sub-voxel-sized features. This results in partial volume effects: middling grayscale values in voxels that contain both pore and rock material (e.g., at pore boundaries), and interpretation of these poorly defined edges can be highly subjective. Noise from a number of sources (the X-ray source, the detector, the sample holder, etc.) is inherent to XCT image collection (Leu et al. 2014). High noise levels can cause misclassification, particularly if global thresholding is used for segmentation and image contrast is low. Filters attempt to correct for these factors in order to improve image quality and simplify the segmentation process.

Prior works have analyzed the impact of image enhancement protocols on digital rock properties. Müter et al. (2012) found that segmentation using Otsu thresholding was improved by the application of edge-enhancing and noise-reducing filters, especially at high levels of Gaussian blurring. Sell et al. (2016) tested numerous noise reduction and edge detection filters and found that gas hydrate saturation levels calculated from CT imagery were significantly impacted by the image enhancement protocols prior to segmentation by combined watershed and region growing techniques. Shulakova et al. (2013) compared signal-to-noise ratios after application of various noise suppression filters and found that an edge-preserving filter optimized noise reduction while maintaining important feature boundaries.

In this study, a dual filter approach was employed to address these CT imaging artifacts, coupling contrast enhancement and noise reduction filters. Prior work suggests that dual filtering can improve segmentation results in rocks with complex pore networks and feature sizes near voxel resolution and that applying a noise reduction filter without first applying a contrast enhancement filter leads to erasure of small features (Müter et al. 2012). Here, an unsharp mask was used to enhance contrast at pore-rock boundaries, followed by an edge-preserving bilateral filter to reduce blur and noise (Ushizima et al. 2011). Anisotropic diffusion and median filtering were also considered as noise reduction filter options, but both can suffer instability and inefficiency because they solve partial differential equations iteratively. Bilateral filtering uses range and domain filtering and is therefore a preferred method for large datasets (Tomasi and Manduchi 1998). In a comparative study using images with a resolution of less than 5 μm, a bilateral filter outperformed a median filter (med3) when Gaussian noise had low variance ($\sigma < 75$), and at three times the speed (Ushizima et al. 2011). Because of the low Gaussian noise variance and large size of the XCT dataset used in this study, a bilateral filter was selected.

Beam hardening is another inherent artifact of bench-scale XCT imaging. Bench-scale XCT instruments use a polychromatic beam of X-rays, and the beam's lower frequencies are preferentially attenuated as it passes through the sample material. The result is a relatively high-frequency, high-energy (hardened) beam. A beam passing through the center of a sample (i.e., a greater amount of material in a cylindrical sample) has hardened by the time it passes through the bulk of the material, reducing the effective attenuation coefficient of the center material compared to that of the edges. Upon reconstruction, this manifests as brightening near the edges of the sample. The segmented dataset then shows artificial radial variation in local porosity. Reconstruction XCT software can reduce beam hardening, but programs often over- or under-correct. Synchrotron XCT instruments, which use a monochromatic beam, do not produce this artifact (Wildenschild and Sheppard 2013). But because synchrotron facilities are not widely available, beam hardening correction is important for most XCT users. Khan et al. (2015) developed an algorithm specifically for cylindrical rock cores that fits a 2D quadratic polynomial for removal of beam hardening

artifacts in classically filtered back-production reconstructed slices. Their code was adapted for the scans used in this study.

The purpose of this study is to introduce and assess a pre-segmentation image filtering workflow to improve the reproducibility of the TWS output and therefore the confidence in rock behavior predictions based on XCT data. To evaluate the effectiveness of the proposed workflow, XCT scans of three rock core samples were examined. Porosities were computed from the dataset after various filter combinations were applied, and those values were compared to experimental measurements. Further investigation into additional rock parameters—pore size distribution and permeability—was performed in a case study of one rock core scan. From the segmented dataset, a computational mesh of the pore space was generated, and flow was simulated using OpenFOAM to estimate permeability (OpenFOAM 2019). Digitally derived values were validated using an experimental flow-through permeability test. The results of this study support the hypothesis that the application of these three filters prior to the definition of training sets for TWS results in improved output consistency.

2 Methods

2.1 Laboratory Methods

This study analyzed three core samples of 5.1 cm length × 2.5 cm diameter, all purchased from Kocurek Industries. The cores included: Indiana Limestone, a carbonate from the Mississippian period; Edwards Limestone, a more heterogeneous carbonate from the Lower Cretaceous; and Upper Devonian Berea Sandstone. Kocurek provided expected mineral characteristics for the samples based on analysis of other cores in their inventory (Table 1).

An XCT scan of each core was taken in the Computed Tomography in Earth and Environmental Sciences (CTEES) facility at the University of Michigan, using a Nikon XT H 225 ST industrial CT scanner. The voxel resolution of each scan was 28 µm; additional scan parameters are included in the Supplementary Information. The XCT dataset was reconstructed using Nikon CT Pro 3D software, and the built-in beam hardening correction was applied.

Mercury intrusion porosimetry (MIP) was used to determine porosity and pore size distribution experimentally. MIP was performed on material of the same type and from the same supplier using a Micromeritics AutoPore V in the Biointerfaces Institute at the University of Michigan. Two to three intact cubes of rock material, each roughly 1 cm^3, were inserted into the penetrometer bulb. The total sample mass was 3.102 g, 3.2441 g, and

Table 1 Expected rock properties provided by sample supplier

Sample	Expected porosity (%)	Expected permeability (mD)	Mineral content
Indiana limestone	14–18	16–20	97% Calcite, 3% Montmorillonite
Edwards limestone	33–35	65–85	100% Calcite
Berea sandstone	20–22	370–400	91% Quartz, 9% Kaolinite

1.8954 g for Indiana Limestone, Edwards Limestone, and Berea Sandstone, respectively. The porosimeter took measurements at 50 different target pressures ranging from 3400 Pa to 4.2×10^8 Pa. Volume distribution results were compared to digital results.

Core permeability for the Indiana Limestone sample was determined experimentally using a high-pressure flow-through apparatus. Water maintained a confining pressure of 13.8 MPa around the core at ambient temperature. Deionized water flowed through the core at a constant flow rate of 1 mL/min. Upstream and downstream pressure transducers continuously monitored fluid pressure upstream and downstream of the core. Permeability was calculated based on this pressure differential using Darcy's Law.

2.2 Image Preparation, Filtering, and Segmentation

Each CT dataset was first prepared for filtering. All steps of initial image preparation were performed using Fiji, an install of ImageJ bundled with many image processing plugins (Schindelin et al. 2012). The incomplete image slices at the very ends of the cores were cropped out of the dataset, resulting in a 1050-slice TIFF stack with 1000×1000 pixels per slice. The Analyze Particles function generated a silhouette mask of the core for each image slice. When this mask was multiplied by the original dataset and the threshold was adjusted, the background voxels all assumed a grayscale value of 0. This allowed analysis of the core in isolation from background interference.

Following initial image preparation, eight different combinations of filters were applied to the dataset prior to training class definition in order to assess their influence on the variability of segmentation results. The combinations tested are listed in Table 2 and are described in more detail below. For each filter combination, eight repetitions of training set definition and TWS classification were performed.

Unsharp mask filter: An unsharp mask with a Gaussian blur radius (σ) of 5 pixels and a mask weight of 0.4 was subtracted from the original image in order to enhance feature edges. These values were selected based on the conclusions of Müter et al. (2012), who found that segmentation results were optimal at σ values between 3 and 5, and that the results were not very sensitive to changes in either input parameter.

Bilateral filter: The algorithm described by Ushizima et al. (2011) was used for parameterization of the bilateral filter. This method turns patches of regions of interest (ROI) into parameters for the bilateral filter. Ten to fifteen ROIs of known material were defined, and Fiji was used to calculate the mean and standard deviation of XCT values within each

Table 2 Image filter combinations applied prior to TWS

Task	Unsharp mask filter (Un)	Bilateral filter (Bil)	Beam hardening correction (BH)	Trainable Weka segmentation
1				**X**
2	**X**			**X**
3	**X**	**X**		**X**
4	**X**	**X**	**X**	**X**
5			**X**	**X**
6		**X**		**X**
7		**X**	**X**	**X**
8	**X**		**X**	**X**

ROI. These were input into the Matlab script FindSigmaR (see Supplementary Information Sect. 4), which outputted a σ_r value for the bilateral filter. Here σ_r represents the range of voxel intensities, which is assumed to be equal to the largest intensity variation within any ROI. The bilateral filter spatial domain parameter, σ_d, was assigned a value of 3 (Ushizima et al. 2011).

Beam hardening correction: A built-in beam hardening correction was applied during reconstruction using Nikon CT Pro 3D, but the output datasets showed beam hardening overcorrection. A Matlab script (see Supplementary Information Sect. 5) adapted from Khan et al. (2015) was applied to fit a polynomial function to the XCT dataset and remove beam hardening artifacts. Figure 1 demonstrates the improvement: it shows the average XCT value at varying radial distances from the center of the core in one image, before (red triangles) and after (blue circles) this script was applied. Before the script was applied, the image had radially decreasing XCT values: the edge was darker than the center of the core. After the script was applied, the values were more uniform. Linear regressions were fit to the datasets of each to illustrate the differences in slope.

A filtering workflow diagram for the fully filtered (Un + Bil + BH) case, and an image showing the effects of these filters, is shown in Fig. 2.

After the beam hardening correction, training sets were defined. Using the freehand selection tool in TWS, a user selected three regions in each of pore and rock space and added them to the training classes. The user did not select the same pixels each time; rather, they identified features (i.e., a single pore, or a single mineral grain) from the dataset on a case-by-case basis in order to allow for user bias in feature selection. The resulting training classes were approximately 100–200 pixels each. An example demonstrating the type of training data selected and associated segmentation results is shown

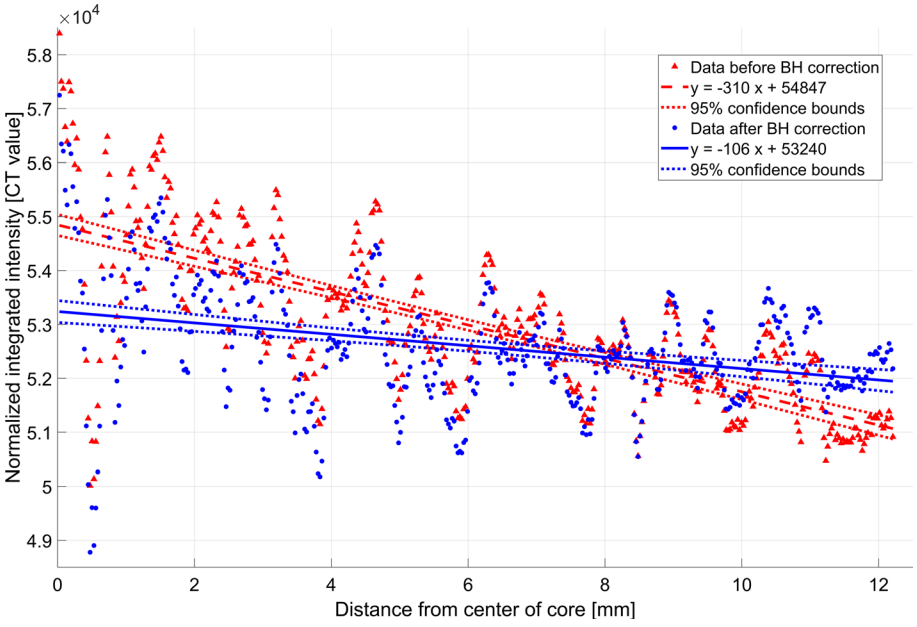

Fig. 1 Average intensity by radial distance of one XCT image slice, with beam hardening correction done by XCT software (red triangles) and correction done by Khan et al. (2015) Matlab code (blue circles). Linear regressions and their 95% confidence intervals are shown for each dataset

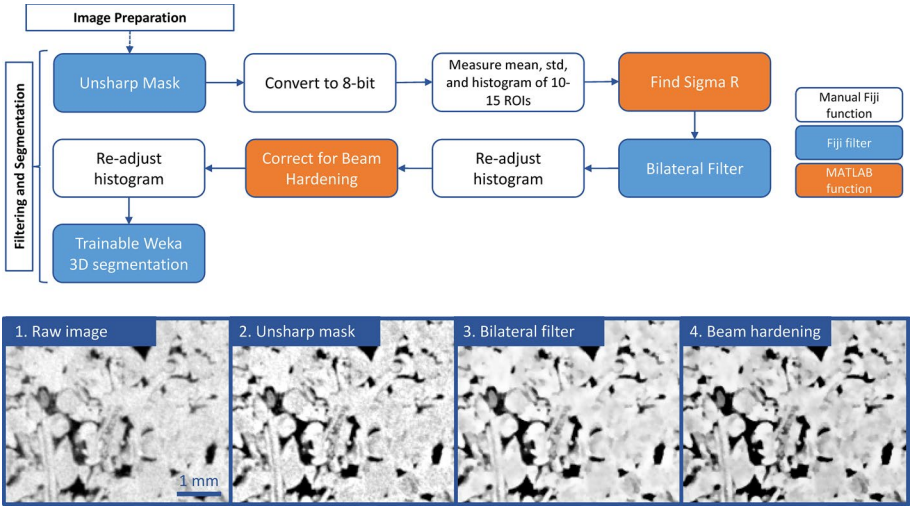

Fig. 2 Top: Image filtering and segmentation workflow. Completed with manual Fiji functions, Fiji filters, and Matlab scripts (see Supplementary Information for code). Bottom: A series of images showing the effects of each filter on a small section of the CT dataset

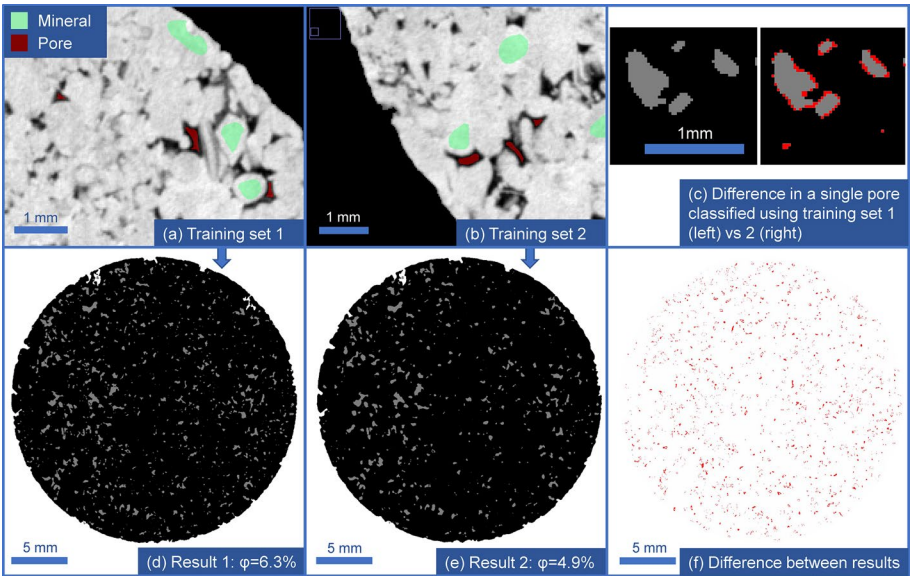

Fig. 3 An example illustrating different segmentation results (**d** and **e**) based on different sample training sets (**a** and **b**). The red and green regions are regions that the user defined as pore and mineral, respectively. **c** shows the differences at the pore level in pore size and connectivity, and (**f**) shows the difference in pore pixel assignment of the full image

in Fig. 3 (note that this example is for illustrative purposes only; training data used for the study were selected from different spatial regions across the dataset). These training data were used to classify the full image using TWS.

2.3 Indiana Limestone Pore Size Distribution

Pore volume distributions computed from the segmented Indiana Limestone datasets were compared to experimental results. To digitally quantify the pore volume distribution, the methods described in Münch et al. (2006) were used. The Disconnect Particles plugin was used to disconnect pores at their bottlenecks, with a k value of 0.7. This value, k, is a nondimensional parameter between 0 and 1 that defines the allowable degree of constriction above which pores are defined as distinct. It is a function of the relative radii of the pores and their constriction points, and the value was selected based on visual inspection. To measure the volume and radius of each pore in 3D (assuming spherical pores), the Particle Size Distribution plugin was used (Münch et al. 2006). A substack of the first 200 image slices was used for each iteration to decrease processing time.

2.4 Indiana Limestone Permeability Simulation

From a subsection of the segmented Indiana Limestone dataset, the BoneJ plugin for Fiji generated a surface file for the solid (Doube et al. 2010). The boxMesh utility for OpenFOAM was used to create a uniform cubic grid cell structure enclosing the surface file domain. The snappyHexMesh mesh generator identified and extracted surface features from the surface file, refined the mesh near those features, and then "snapped" the mesh to the surface file, thus creating a computational mesh of the negative (pore) space for flow simulation. The substack started at the same slice for each iteration, but the length of the substack varied from 50 to 500 slices (1.4–14 mm) in order to achieve snappyHexMesh breakthrough at a constant box mesh resolution of one grid cell per voxel. This mesh resolution was limited by computational processing ability. Steady-state, nonreactive flow through the mesh was simulated using simpleFoam (OpenFOAM 2019). Boundary conditions were defined to mimic the laboratory experimental permeability conditions described in Sect. 2.1. No-slip conditions were applied to the four side walls and to the grain-fluid interface. Pressure at the outlet was held constant at

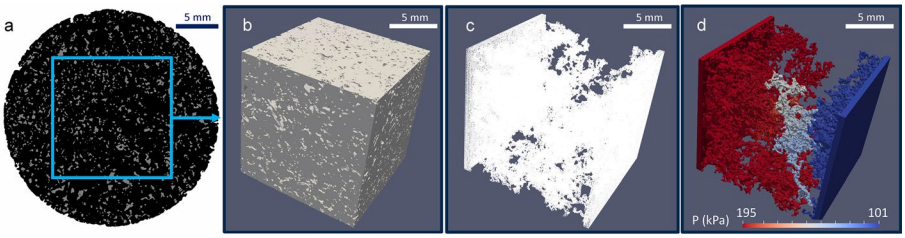

Fig. 4 OpenFOAM permeability simulation setup. **a** Subsection was taken from binarized segmented dataset. **b** Surface file of rock material was generated. **c** Mesh was generated in OpenFOAM using blockMesh and snappyHexMesh. **d** simpleFoam was run and pressure difference was used to infer permeability. See Online Resource 1–3 for animated versions

atmospheric pressure, and pressure at the inlet was calculated during flow. Water was flooded through the domain at a rate of 1 mL/min. Steady-state inlet pressure was observed, and permeability was determined using Darcy's Law. Figure 4 illustrates the model setup.

3 Results and Discussion

3.1 Overall Porosity

Figure 5 shows overall porosity results for the segmented datasets, grouped by filter combination. Box plots of the Indiana Limestone, Edwards Limestone, and Berea Sandstone core data are shown in purple, yellow, and dark blue, respectively. The median value is illustrated with a red line, the boxes represent the 25th–75th percentiles, and whiskers show the most extreme values that are not outliers. Outliers are defined here as points that fall more than 1.5 interquartile ranges (IQR) outside the box. Additional data from a higher-resolution scan of Berea Sandstone material (described in more detail below) are shown in light blue. Experimental porosity values from MIP are shown with dashed lines.

A few patterns arise that are consistent between the two limestone samples (Indiana Limestone in purple and Edwards Limestone in yellow): the fully filtered (Un + Bil + BH) datasets show higher average porosity and reduced variance compared to the unfiltered (None) case. The cases closest to experimental values are the (Un + BH)

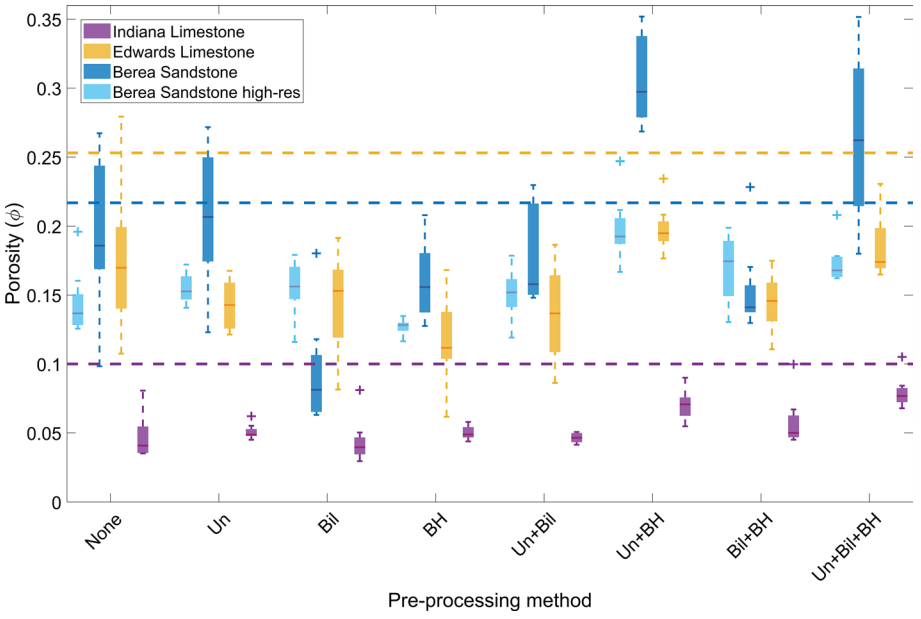

Fig. 5 Box-and-whisker plots showing porosity values from segmented datasets processed using various filter combinations. The red line shows the median, the boxes contain the 25th–75th percentiles, and outliers fall more than 1.5 IQR outside the boxes. The dashed lines show experimental porosity determined by MIP. Un = unsharp mask, Bil = bilateral filter, and BH = beam hardening correction. $n = 8$ for each filter combination

and (Un + Bil + BH) cases. The similarity between the (Un + BH) and (Un + Bil + BH) cases, along with the fact that the bilateral filter alone shows little change from the unfiltered dataset data, suggests that the bilateral filter is relatively unimportant for these datasets. The bilateral filter is applied to reduce noise; this suggests that noise in these datasets contributes less to segmentation output variability than poor edge definition and beam hardening artifacts do. These data also suggest that the unsharp mask is particularly important for narrowing the range of values obtained through segmentation. All values, regardless of filter method, are lower than the experimental value found using MIP. This is most likely due to the presence of sub-voxel porosity in the relatively low-resolution datasets. The digital method is unable to resolve pores smaller than 1 pixel (28 μm, in this study) in radius. If a particular voxel contains, for example, 40% pore space and 60% mineral, it will be classified as mineral. The presence of small pores is therefore consistent with an underestimation of bulk porosity.

Initial analysis of the Berea Sandstone (dark blue) core scan shows quite different results. Variance is not reduced through the use of the three filters. The (Un + BH) and (Un + Bil + BH) cases again give the highest porosity values, but in this case, they are overestimates compared to the experimental data. It is suspected that these inconsistent results are due, at least in part, to the small grain and pore size of this rock material. All three core scans used the same voxel resolution, which was sufficient to identify distinct pore and mineral regions in the limestone samples. The grain size of the sandstone was close to the voxel resolution of the scan, making it more vulnerable to partial volume effects and therefore more challenging to identify training regions that were wholly made up of pore or mineral.

A small (~ 1 cm^3) rough block of Berea Sandstone material was scanned at higher resolution (8 μm per voxel), and the study was repeated on this scan. The results are shown in light blue and referred to as "high-res scan." This case shows more similar results to the limestone example. The (Un + BH) and (Un + Bil + BH) cases show the closest values to the MIP porosity (shown with a dark blue dashed line), with the (Un + BH) case providing a slightly closer value to the measured porosity. Variance is lower in the (Un + Bil + BH) case than the (None) case. As described above, the beam hardening correction used in this study was specifically written for cylindrical core samples, so it was not being used as designed when applied to a non-cylindrical sample. It appeared to have similar effect on this rough chunk of material as was seen in the cylindrical limestone samples.

The study of the Berea Sandstone highlights the importance of selecting high enough scan resolution to allow for precise and reliable segmentation of an XCT dataset. The tradeoff between sample size and scan resolution is a physical limitation of the benchtop XCT scanner. The voxel resolution of the core samples analyzed in this study was the highest-possible resolution that allowed for capture of the entire core height. These data may recommend a secondary, higher-resolution scan, as well as experimental methods, to validate segmentation results of a low-resolution scan.

Only three regions in each of pore space and mineral space (six total regions) were used to define the training classes for TWS input, because increased amounts of training data corresponded to prohibitively high processing times. A prior work compared TWS outputs using varying numbers of training regions and found that 10 regions were preferable to 3 for their segmentation of SEM data for crystal size distribution analysis (Lormand et al. 2018). In order to ensure that the limited training dataset size used here did not falsely skew the porosity results, an additional analysis was performed to test varying numbers of training regions. A single filtered dataset of the Indiana Limestone scan (Un + Bil + BH)

was used and segmentation was performed using 6, 20, 30, and 40 training regions (divided evenly between pore and mineral regions). This process was repeated three times for each number of regions. Results are shown in Supplementary Information Sect. 2. A pairwise *t*-test was performed at the $\alpha = 0.05$ level to compare the 6-ROI mean porosity to the 20-, 30-, and 40-ROI mean porosities, respectively. Likewise, a pairwise f-test was performed at the $\alpha = 0.05$ level to compare variances. No significant differences in mean or variance were found at this confidence level. These results suggest that the porosity results obtained in this study would not have differed significantly had more training regions been used.

A sensitivity analysis was performed for the Indiana Limestone (Un + Bil + BH) case on the three filter parameters that had been selected based on prior works. This included the bilateral filter spatial radius (BS), the unsharp mask Gaussian blur radius (UR), and the unsharp mask weight (UW). In order to reduce processing time, the analysis was performed on a 100-slice substack from the center of the dataset. This substack length was deemed to be statistically representative of the full dataset: for $n = 10$ 100-slice stacks, the coefficient of variation (i.e., the standard deviation normalized by the mean) was less than 10% (Zhang et al. 2000). The base case (BS = 3, UR = 5, UW = 0.4) was compared to test cases with one changed parameter, with eight repetitions each. Results are shown in Fig. 6.

Pairwise t- and f-tests at the $\alpha = 0.05$ were used to compare mean and variances of the base case against each test case. The bilateral filter spatial radius (red) had no significant difference in mean or variance at this confidence level for any of the tested values. As discussed above, the bilateral filter had little effect on the results from the full core analyses, and this sensitivity analysis suggests that this finding would hold true even after changing

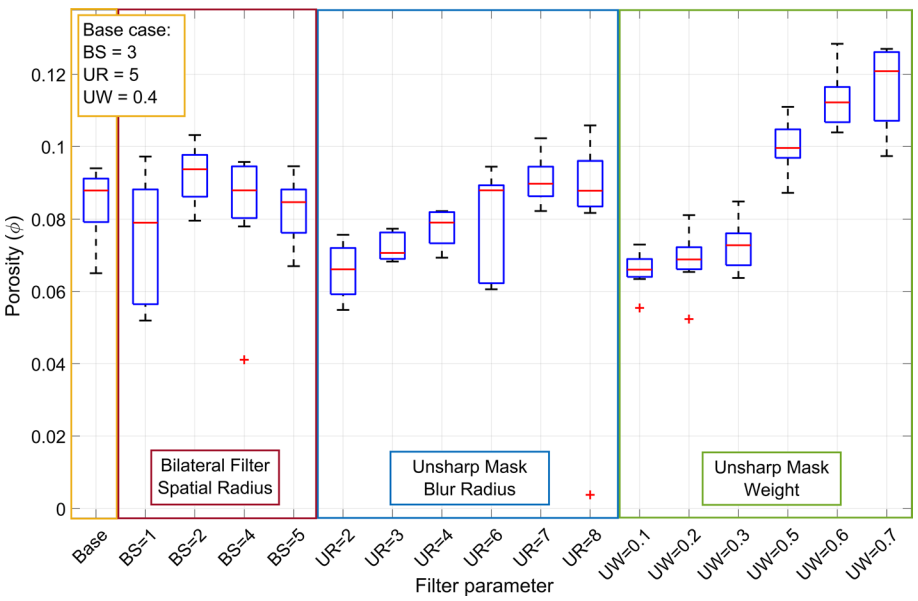

Fig. 6 Box-and-whisker plot results of filter parameter sensitivity analysis. A base case (yellow) was compared to cases in which one parameter value was changed: bilateral filter spatial radius (red), unsharp mask blur radius (blue), or unsharp mask weight (green). Red lines show medians, boxes show 25th–75th percentiles, and whiskers show most extreme values that are not outliers. Outliers (red plus signs) are points that fall further than 1.5 IQR outside of the box

the bilateral filter parameters. The unsharp blur radius (blue) had significantly different mean values for the UR = 2 and UR = 3 cases, but at UR ≥ 4 no significant difference from the base case was observed. The variance was lower in the UR = 3 case, higher in the UR = 8 case (due to one far outlier), and otherwise not significantly different from the base case. These results suggest that using a blur radius above a minimum value is important, but above that point, the value does not make a difference. The largest difference was observed in the unsharp mask weight (green) test cases. Each case had a different mean value from the base case, increasing from the lowest value for the lowest mask weight to the highest value for the highest mask weight. Variance was consistent across all cases. These data suggest that a mask weight of 0.5 would have been better suited for this particular rock core, as the mean of the UW = 0.5 test case was closest to the experimental porosity of 0.10. This highlights the value of a pre-analysis testing different filter parameters on a representative sub-volume in order to optimize filtering on a case-by-case basis.

3.2 Indiana Limestone Pore Size Distribution

As a case study on the Indiana Limestone core scan, pore volume distributions were generated based on the digitally derived data and experimental MIP data (Fig. 7). Digital data were binned based on the size thresholds of the porosimeter in order to compare volume fractions. The distributions calculated from the XCT data show little variance compared to the experimental data. Pores with radii around 50–500 µm (roughly 2–18 voxels) dominate the pore volume fraction. The full MIP dataset (black dotted line) shows a much wider distribution of sizes, with approximately 23% of the pore volume fraction made up of submicron pores. This figure highlights that, as expected, comparison between digital and

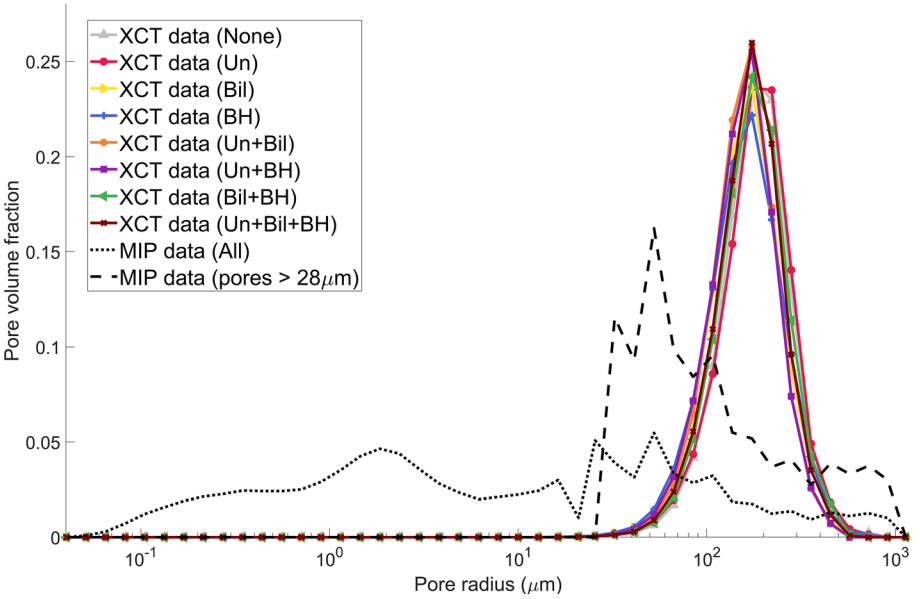

Fig. 7 Pore volume distribution as a function of pore radius. Digitally derived distributions for each filtered combination are shown in solid lines. Experimental MIP data are shown including all pores (black dotted line) and only pores bigger than the voxel size of the XCT data (black dashed line)

experimental data is hampered by difference in resolution (Nimmo 2004). Digital analysis is unable to resolve pores smaller than 1 XCT voxel, whereas MIP can detect pores down to 10 s of nm. We see very little difference between the XCT datasets with different filter combinations. Image filtering cannot overcome the loss of resolution from bench-scale XCT imaging. Even when MIP data are truncated to only include those pores that the XCT data could possibly resolve (radius greater than 1 XCT voxel), they still have greater variance because of that difference in resolution.

A single-case sensitivity analysis was performed on the impact of the Disconnect Particles parameter, k. The (Un + Bil + BH) datasets were aggregated and analyzed with k values ranging from 0.0 to 1.0 (Fig. 8). More detailed data from this analysis are provided in the Supplementary Information, Sect. 3. The resulting data show that pore size distributions begin to converge at k values above ~ 0.5. Low k values (i.e., low disconnection) correspond with a poorer approximation of the most abundant pore radii found using MIP but a better representation of the largest pores (> 500 µm radius), except for the $k = 0.0$ case (dark red), which severely overestimates the abundance of pores > 1 mm in diameter. These data suggest that k value selection is a tradeoff between nearer estimation of the peak values in the experimental pore size distribution curve and improved representation of the distribution of macropores. Either option could be preferable depending on the use case. The selection of $k = 0.7$ in this study prioritized representation of smaller pores in an effort to represent the pore sizes that dominate the pore volume fraction. No alternative k value selection offers a substantial improvement towards this goal, as this parameter cannot correct for the difference in resolution between experimental data and XCT-derived data.

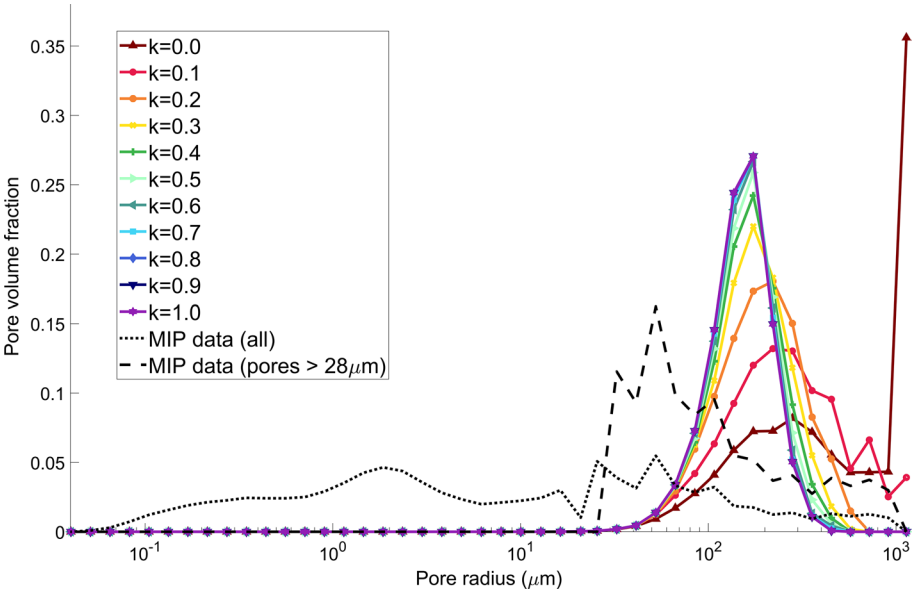

Fig. 8 Sensitivity case study on Disconnect Particles parameter, k, ranging from $k = 0.0$ in dark red (no disconnection of adjacent pores) to $k = 1.0$ in violet (high disconnection)

3.3 Indiana Limestone Simulated Permeability

A case study of permeability simulations was performed on the Indiana Limestone core. In order to explore the reproducibility of simulated permeability values from these segmented datasets, the segmented datasets associated with the maximum, median, and minimum porosity were used to generate computational meshes with which to simulate permeability using OpenFOAM. The range of these values is shown in Fig. 9.

The dataset with all three filters applied shows the smallest range of simulated permeability values. This is likely due to the small range of porosity values derived from this dataset and illustrates that variation in the initial segmentation process can amplify the differences in simulated downstream processes. Porosity variances were also very small for the Un, BH, and Un + Bil datasets, yet these do not show much reduction in simulated permeability range. This discrepancy may be related to differences in pore connectivity rather than porosity itself, which is a topic for further exploration.

These data suggest that the application of the three filters did improve reproducibility of permeability simulations but did not improve estimation of the permeability value itself. The overestimation of permeability compared to experimental data could be partially attributed to the difference in pore size distribution. The higher fraction of larger pore radii seen in the digital pore size distribution is consistent with an overestimation of permeability. This is further evidence that rock parameter predictions derived from bench-scale CT data are affected by low voxel resolution. We would still expect to see improved reproducibility with a higher-resolution scan and may also see an improved permeability value

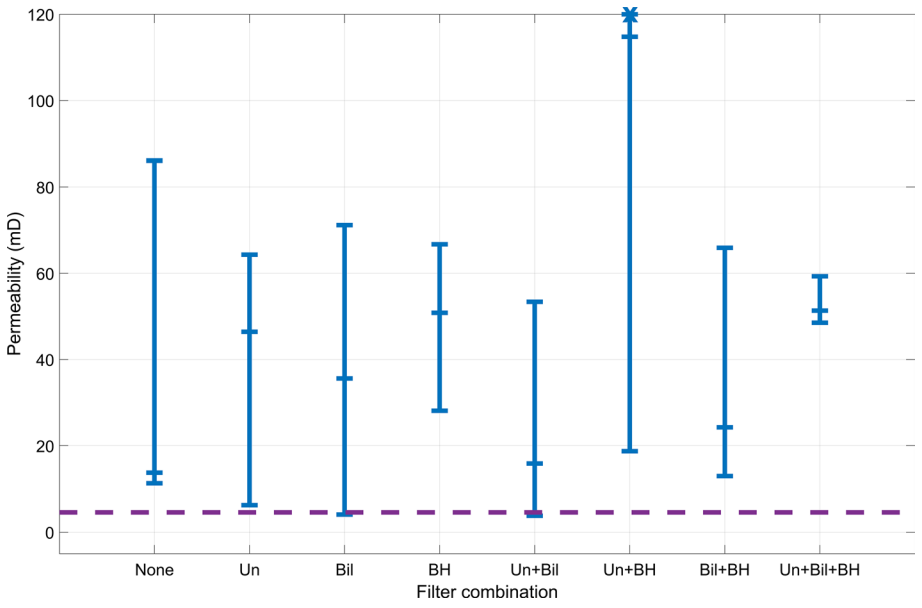

Fig. 9 Simulated permeability ranges from segmented datasets processed using various filter combinations. The markers indicate permeabilities simulated from the maximum, median, and minimum porosity datasets from each filter combination. The asterisk on the Un + BH range shows an outlier value. The dashed purple line shows experimental permeability. *Un*=unsharp mask, *Bil*=bilateral filter, and *BH*=beam hardening correction

estimate. The overestimation of permeability could also be an illustration of limitations of the OpenFOAM simulation. This method seeks to predict permeability, an upscaled parameter, from a subsection of an already small-scale sample. Heterogeneity within the core (which would be likely in a carbonate due to the presence of fossil fragments) could introduce error to the simulated estimates because a substack was used instead of the whole core length. The mesh resolution and subsection length used here were at the upper limits of the computing capability currently in place. Future work will implement high-performance computing resources in order to explore whether increased subsection size and mesh resolution promote agreement between simulated and experimental results.

4 Conclusions

The results of this study support a recommendation to use image filtering prior to the definition of training classes for XCT segmentation by machine learning algorithm. Here, a three-stage workflow was considered for binary segmentation of three core samples: an unsharp mask for contrast enhancement, an edge-preserving bilateral filter for noise reduction, and a beam hardening correction.

In the two limestone samples, the datasets that had all three filters applied had reduced variability in overall porosity and a closer porosity value to the experimental MIP value compared to the unfiltered cases. The XCT data from the sandstone core showed inconclusive results, but segmentation was made difficult due to the scan resolution being close to pore and grain size. A higher-resolution scan of a small sample of the Berea Sandstone showed the same variance reduction and prediction improvement seen in the limestone samples.

Simulated permeability on the Indiana Limestone core also showed an improvement in reproducibility after the application of these three filters. Pore size distribution was studied for the Indiana Limestone core, but the ability to compare these data to experimental results was hampered by differences in resolution between the XCT and MIP analyses. Access to higher-resolution synchrotron XCT instruments is limited for most researchers, and thus there is value in improving the results that can be obtained using the widely available bench-scale XCT.

Improving the reproducibility of XCT segmentation results is essential for many subsurface applications, as this step is critical for the prediction of subsurface fluid behavior. Here, identification of the pore network and its applications for fluid flow were studied in mineralogically simple rock samples. These methods may also assist in the segmentation of different mineral species, which could identify mineral species accessible to fluid-rock interactions. For any application, increasing XCT segmentation consistency and limiting user bias would improve the confidence in any downstream predictions made using those data, as modeling flow through porous media at the reservoir scale depends strongly on information gathered from rock core samples.

Supplementary Information The online version contains supplementary material available at https://doi.org/10.1007/s11242-021-01690-3.

Acknowledgements The authors would like to thank Zixian Wang for her assistance in gathering laboratory results and Eva Albalghiti and three anonymous reviewers for their valuable feedback. Laboratory support: this study includes data produced in the CTEES facility at University of Michigan, supported by the Department of Earth & Environmental Sciences and College of Literature, Science, and the Arts. Mercury

intrusion porosimetry data were collected in the Nanotechnicum lab in the Biointerfaces Institute at the University of Michigan.

Authors' contributions Ellen P. Thompson: Formal analysis, Writing—Original draft, Conceptualization. Kira Tomenchok: Methodology, Conceptualization. Tyler Olson: Investigation. Brian R. Ellis: Supervision, Writing—Review & Editing.

Funding This material is based upon work supported by the National Science Foundation (CAREER Grant No. 1943726) and the Alfred P. Sloan Foundation (Grant No. 2020–12,466). Any opinions, findings, and conclusions or recommendations expressed in this material are those of the author(s) and do not necessarily reflect the views of the National Science Foundation. This research was also supported by the University of Michigan Energy Institute through an Undergraduate Research Opportunities Program fellowship.

Availability of data and material The datasets generated and analyzed during the current study are available from the corresponding author upon request.

Code availability The code used for this study is included in the Supplementary Information.

Declarations

Conflict of interest The authors have no known financial or personal competing interests to declare.

References

Alhammadi, A.M., AlRatrout, A., Bijeljic, B., Blunt, M.J.: Pore-scale imaging and characterization of hydrocarbon reservoir rock wettability at subsurface conditions using X-ray microtomography. JoVE 57915 (2018). https://doi.org/10.3791/57915

Arganda-Carreras, I., Kaynig, V., Rueden, C., Eliceiri, K.W., Schindelin, J., Cardona, A., Sebastian Seung, H.: Trainable Weka Segmentation: a machine learning tool for microscopy pixel classification. Bioinformatics **33**, 2424–2426 (2017). https://doi.org/10.1093/bioinformatics/btx180

Bazaikin, Y., Gurevich, B., Iglauer, S., Khachkova, T., Kolyukhin, D., Lebedev, M., Lisitsa, V., Reshetova, G.: Effect of CT image size and resolution on the accuracy of rock property estimates. J. Geophys. Res. Solid Earth **122**, 3635–3647 (2017). https://doi.org/10.1002/2016JB013575

Deng, H., Fitts, J.P., Peters, C.A.: Quantifying fracture geometry with X-ray tomography: Technique of Iterative Local Thresholding (TILT) for 3D image segmentation. Comput. Geosci. **20**, 231–244 (2016). https://doi.org/10.1007/s10596-016-9560-9

Doube, M., Kłosowski, M.M., Arganda-Carreras, I., Cordelières, F.P., Dougherty, R.P., Jackson, J.S., Schmid, B., Hutchinson, J.R., Shefelbine, S.J.: BoneJ: Free and extensible bone image analysis in ImageJ. Bone **47**, 1076–1079 (2010). https://doi.org/10.1016/j.bone.2010.08.023

Garfi, G., John, C.M., Berg, S., Krevor, S.: The sensitivity of estimates of multiphase fluid and solid properties of porous rocks to image processing. Transp. Porous Med. **131**, 985–1005 (2020). https://doi.org/10.1007/s11242-019-01374-z

Hommel, J., Coltman, E., Class, H.: Porosity-permeability relations for evolving pore space: A review with a focus on (bio-)geochemically altered porous media. Transp. Porous Med. **124**, 589–629 (2018). https://doi.org/10.1007/s11242-018-1086-2

Iassonov, P., Gebrenegus, T., Tuller, M.: Segmentation of X-ray computed tomography images of porous materials: A crucial step for characterization and quantitative analysis of pore structures. Water Resour. Res. 45 (2009). https://doi.org/10.1029/2009WR008087

Khan, F., Enzmann, F., Kersten, M.: Beam-hardening correction by a surface fitting and phase classification by a least square support vector machine approach for tomography images of geological samples. Solid Earth Discuss. **7**, 3383–3408 (2015). https://doi.org/10.5194/sed-7-3383-2015

Leu, L., Berg, S., Enzmann, F., Armstrong, R.T., Kersten, M.: Fast X-ray micro-tomography of multiphase flow in Berea Sandstone: A sensitivity study on image processing. Transp. Porous Med. **105**, 451–469 (2014). https://doi.org/10.1007/s11242-014-0378-4

Lindquist, W.B., Venkatarangan, A., Dunsmuir, J.: Wong, T: Pore and throat size distributions measured from synchrotron X-ray tomographic images of Fontainebleau sandstones. J. Geophys. Res. Solid Earth **105**(B9), 21509–21527 (2000). https://doi.org/10.1029/2000JB900208

Lormand, C., Zellmer, G.F., Németh, K., Kilgour, G., Mead, S., Palmer, A.S., Sakamoto, N., Yurimoto, H., Moebis, A.: Weka Trainable Segmentation plugin in ImageJ: A semi-automatic tool applied to crystal size distributions of microlites in volcanic rocks. Microsc. Microanal. **24**, 667–675 (2018). https://doi.org/10.1017/S1431927618015428

Ma, J.: Review of permeability evolution model for fractured porous media. J. Rock Mech. Geotech. Eng. **7**, 351–357 (2015). https://doi.org/10.1016/j.jrmge.2014.12.003

Mostaghimi, P., Blunt, M.J., Bijeljic, B.: Computations of absolute permeability on micro-CT images. Math. Geosci. **45**, 103–125 (2013). https://doi.org/10.1007/s11004-012-9431-4

Münch, B., Gasser, P., Holzer, L., Flatt, R.: FIB-nanotomography of particulate systems—Part II: Particle recognition and effect of boundary truncation. J. Am. Ceramic Soc. **89**, 2586–2595 (2006). https://doi.org/10.1111/j.1551-2916.2006.01121.x

Müter, D., Pedersen, S., Sørensen, H.O., Feidenhans'l, R., Stipp, S.L.S.: Improved segmentation of X-ray tomography data from porous rocks using a dual filtering approach. Comput. Geosci. 49, 131–139 (2012). https://doi.org/10.1016/j.cageo.2012.06.024

Nimmo, J.R.: Porosity and pore size distribution. In: Hillel, D., Hatfield, J.L. (Eds.), Encyclopedia of Soils in the Environment, pp. 295–303. Elsevier (2004)

OpenFOAM. OpenCFD. https://www.openfoam.com/ (2019)

Pini, R., Madonna, C.: Moving across scales: a quantitative assessment of X-ray CT to measure the porosity of rocks. J. Porous Mater. **23**, 325–338 (2016). https://doi.org/10.1007/s10934-015-0085-8

Schindelin, J., Arganda-Carreras, I., Frise, E., Kaynig, V., Longair, M., Pietzsch, T., Preibisch, S., Rueden, C., Saalfeld, S., Schmid, B., Tinevez, J.-Y., White, D.J., Hartenstein, V., Eliceiri, K., Tomancak, P., Cardona, A.: Fiji: an open-source platform for biological-image analysis. Nat. Methods **9**, 676–682 (2012). https://doi.org/10.1038/nmeth.2019

Sell, K., Saenger, E.H., Falenty, A., Chaouachi, M., Haberthür, D., Enzmann, F., Kuhs, W.F., Kersten, M.: On the path to the digital rock physics of gas hydrate-bearing sediments – processing of in situ synchrotron-tomography data. Solid Earth **7**, 1243–1258 (2016). https://doi.org/10.5194/se-7-1243-2016

Shulakova, V., Pervukhina, M., Müller, T.M., Lebedev, M., Mayo, S., Schmid, S., Golodoniuc, P., Bastos De Paula, O., Clennell, M.B., Gurevich, B.: Computational elastic up-scaling of sandstone on the basis of X-ray micro-tomographic images. Geophys Prospecting **61** (2), 287–301 (2012). https://doi.org/10.1111/j.1365-2478.2012.01082.x

Tomasi, C., Manduchi, R.: Bilateral filtering for gray and color images. In: Sixth International Conference on Computer Vision (IEEE Cat. No.98CH36271). Presented at the IEEE 6th International Conference on Computer Vision, Narosa Publishing House, Bombay, India, pp. 839–846 (1998). https://doi.org/10.1109/ICCV.1998.710815

Ushizima, D., Parkinson, D., Nico, P., Ajo-Franklin, J., MacDowell, A., Kocar, B., Bethel, W., Sethian, J.: Statistical segmentation and porosity quantification of 3D x-ray microtomography, in: Tescher, A.G. (Ed.). Presented at the SPIE Optical Engineering + Applications, San Diego, California, USA, pp. 813502 (2011). https://doi.org/10.1117/12.892809

Wildenschild, D., Sheppard, A.P.: X-ray imaging and analysis techniques for quantifying pore-scale structure and processes in subsurface porous medium systems. Adv. Water Resour. **51**, 217–246 (2013). https://doi.org/10.1016/j.advwatres.2012.07.018

Zhang, D., Zhang, R., Chen, S., Soll, W.E.: Pore scale study of flow in porous media: Scale dependency, REV, and statistical REV. Geophysical Res. Letters **27**(8), 1195–1198 (2000). https://doi.org/10.1029/1999GL011101